Distinct Impacts of El Niño-Southern Oscillation and Indian Ocean Dipole on China's Gross Primary Production

Ran Yan[1,2], Jun Wang[1,2*], Weimin Ju[1,2*], Xiuli Xing[3], Miao Yu[4], Meirong Wang[4], Jingye Tan[1,2], Xunmei Wang[1,2], Hengmao Wang[1,2], Fei Jiang[1,2]

[1]Frontiers Science Center for Critical Earth Material Cycling, International Institute for Earth System Science, Nanjing University, Nanjing, Jiangsu 210023, China

[2]Jiangsu Provincial Key Laboratory of Geographic Information Science and Technology, Key Laboratory for Land Satellite Remote Sensing Applications of Ministry of Natural Resources, School of Geography and Ocean Science, Nanjing University, Nanjing, Jiangsu 210023, China

[3]Department of Environmental Science and Engineering, Fudan University, No. 2005, Songhu Road, Yangpu District, Shanghai 200438, China

[4]Joint Center for Data Assimilation Research and Applications/Key Laboratory of Meteorological Disaster, Ministry of Education/Joint International Research Laboratory of Climate and Environment Change (ILCEC)/ Collaborative Innovation Center ON Forecast and Evaluation of Meteorological Disasters, Nanjing University of Information Science and Technology, Nanjing 210044, China

Corresponding author: Jun Wang (wangjun@nju.edu.cn); Weimin Ju (juweimin@nju.edu.cn)

Abstract

Gross primary production (GPP) stands as a crucial component in the terrestrial carbon cycle, greatly affected by large-scale circulation adjustments. This study explores the influence of El Niño-Southern Oscillation (ENSO) and Indian Ocean Dipole (IOD) on China's GPP, utilizing long-term GPP data generated by the Boreal Ecosystem Productivity Simulator (BEPS). Partial correlation coefficients between GPP and ENSO reveal substantial negative associations in most parts of western and northern China during the September-October-November (SON) period of ENSO development. These correlations shift to strongly positive over southern China in December-January-February (DJF), then weaken in March-April-May (MAM) in the following year, eventually turning generally negative over southwestern and northeastern China in June-July-August (JJA). In contrast, the relationship between GPP and IOD basically exhibits opposite seasonal patterns. Composite analysis further confirms these seasonal GPP anomalous patterns. Mechanistically, ~~we ascertain that, in general,~~ these variations are predominantly controlled by soil moisture during ENSO events (except MAM)~~in SON and JJA, but~~ and by temperature during IOD events (except SON) ~~in DJF and MAM~~. Quantitatively, China's annual GPP demonstrates modest positive anomalies in La Niña and negative ~~n~~IOD years, in contrast to minor negative anomalies in El Niño and positive ~~p~~IOD years. This results from counterbalancing effects with significantly greater GPP anomalous magnitudes in DJF and JJA. Additionally, the relative changes in total GPP anomalies at the provincial scale display an east-west pattern in annual variation, while the influence of IOD events on GPP presents an opposing north-south pattern. We believe that this study can significantly ~~contribute to~~ enhance our ~~comprehension~~ understanding of specific processes by which large-scale circulation influences climate conditions and, in turn, affects China's GPP. ~~how intricate atmospheric dynamics influence China's GPP on an interannual scale.~~

Key words: Gross primary production, China, El Niño-Southern Oscillation, Indian Ocean Dipole, BEPS

~~**Highlight**~~

~~(1) Impacts of ENSO and IOD on China's GPP vary with seasons, showing nearly opposite patterns.~~

~~(2) Soil moisture controls GPP in fall and summer, while temperature plays a key role in winter and spring.~~

~~(3) Counterbalancing causes modest positive GPP anomalies in La Niña and nIOD, contrasting with minor negative anomalies in El Niño and pIOD.~~

1.Introduction

Vegetation photosynthesis, a pivotal physiological process affecting the terrestrial carbon cycle, predominantly governs variations in the net biome productivity (NBP), surpassing the impact of total ecosystem respiration (Piao et al., 2020; Wang et al., 2022; Wang et al., 2018). Gross primary production (GPP) represents the total amount of carbon dioxide assimilated by plants per unit time through the photosynthetic processes, acting as a crucial carbon flux in mitigating anthropogenic CO_2 emissions (Gough, 2012; Houghton, 2007). However, despite evident long-term increasing trends in GPP, primarily attributed to CO_2 fertilization (Ryu et al., 2019; Schimel et al., 2015; Yang et al., 2022), it also shows regional and global interannual variations. These variations are largely linked to climate fluctuations driven by ocean-atmosphere interactions and the teleconnections (Wang et al., 2021b; Ying et al., 2022). To date, the impact of such teleconnections on China's GPP remains insufficiently documented.

The El Niño-Southern Oscillation (ENSO) exerts a significant influence on the global terrestrial carbon cycle, which is the dominant mode of inter-annual climate variability (Bauch, 2020; Kim et al., 2017; Wang et al., 2016; Wang et al., 2018; Zeng et al., 2005). Within this context, GPP typically assumes a leading role in shaping the response of terrestrial carbon sinks to ENSO events (Ahlstrom et al., 2015; Wang et al., 2018; Zhang et al., 2018). Global patterns reveal a negative GPP anomaly of approximately −1.08 Pg C yr^{-1} during El Niño years,

contrasting a positive GPP anomaly of about 1.63 Pg C yr^{-1} in La Niña years (Zhang et al., 2019). However, the impact of ENSO on GPP exhibits significant regional differences. At present, while existing researches have predominantly focused on the response of tropical GPP to ENSO, studies specific to China are relatively limited. Liu et al. (2014) highlighted the effects of ENSO on crop growth in the North China, and Li et al. (2021) demonstrated that the response of GPP to El Niño varies with the phase of the Pacific Decadal Oscillation (PDO) in the eastern China.

ENSO is not the sole global climatic oscillation, influencing the terrestrial carbon cycle. Another significant player is the Indian Ocean Dipole (IOD), a tropical coupled ocean-atmosphere mode (Saji et al., 1999), which also affects the terrestrial carbon cycling by modulating the climate circulations (Wang et al., 2022; Wang et al., 2020; Wang et al., 2021b; Yan et al., 2023). Research indicates that IOD events can influence precipitation in China, with effects lasting from the year of the event through the subsequent summer (Zhang et al., 2022a). Zhang et al. (2022b) also proved that extreme positive IOD (pIOD) events in 2019 affected the precipitation in summer 2020 in Eastern China, and proposed that the summer precipitation in the following year was mainly affected by IOD in northern China, while by ENSO in the Yangtze River Basin. Additionally, a prior study explored the influence of the extreme ~~positive IOD (~~pIOD~~)~~ event in 2019 on GPP anomalies across the Indian Ocean rim countries. It suggested a conspicuous negative GPP anomaly occurred in eastern China during the September-October-November (SON) (Wang et al., 2021b).

The primary objective of this study was to comprehensively assess the impact of ENSO and IOD events on GPP in China. To this end, we initially employed partial correlation analysis to elucidate the relationship between GPP and climate anomalies, specifically soil moisture and temperature, induced by ENSO and IOD events across various seasons. The analysis utilized historical long-term GPP data spanning from 1981 to 2021, simulated by the Boreal Ecosystem Productivity Simulator (BEPS) model. The aim was to get a preliminary understanding of the

influence exerted by ENSO and IOD. Furthermore, composite analysis was adopted to illustrate the actual responses during distinct events, including individual ENSO and IOD occurrences. The ensuing discussion will delve into the analysis results on national, regional, and provincial scales.

2.Datasets and methods

2.1 Datasets used

The sea surface temperature (SST) dataset are derived from the Monthly NOAA's Extended Reconstructed Sea Surface Temperature version 5 (ERSSTv5) (Muñoz, 2019). It is generated on a 2°x2° grid, using statistical methods to enhance spatial completeness. Commencing from January 1854 to the present, the monthly SST data includes anomalies computed with respect to a 1971-2000 monthly climatology.

Meteorological data were adopted from ECMWF Reanalysis v5 (ERA5)~~ERA5~~-Land monthly averaged data with 0.1° × 0.1° grids, including 2m surface air temperature (TAS), and volumetric soil moisture (SM) during the period from 1981 to 2021. ERA5-Land was created by replaying the land component of the ECMWF ERA5 climate reanalysis at a higher resolution compared to ERA5. Reanalysis combines model data with global observations into a consistent dataset based on the laws of physics. The original soil moisture data was divided into four layers based on different surface depths. These layers were depth-weighted and then aggregated into the average soil moisture to a depth of 289cm (m^3 m^{-3}).

GPP spanning from 1981 to 2021 was simulated by the BEPS model, featuring a horizontal resolution of 0.0727° × 0.0727°. The BEPS model, originally developed for Canadian boreal ecosystems, has been re-constructed for GPP simulations on the global scale (Chen et al., 1999; Chen et al., 2012). BEPS is a process-based model driven by satellite-observed leaf area index

(LAI), meteorological data, land cover types, soil texture, and CO_2 concentration to simulate the daily carbon flux of terrestrial ecosystems (Chen et al., 2019; Liu et al., 1997). The input data used to drive GPP in this study include ERA5 meteorological data (Hersbach et al., 2023), GLOBMAP LAI product (Liu et al., 2012), Land Cover Classification System (LCCS) generated by the Food and Agriculture Organization (FAO) of the United Nations (Friedl and Sulla-Menashe, 2019), Harmonized World Soil Database v1.2 from FAO (Fischer et al., 2008), and CO_2 concentration based on the Global Monitoring Laboratory from NASA (Lan et al.). Notably, BEPS distinguishes itself from other models through the organic combination of remote sensing data and mechanistic modelling. It produces simulation datasets for GPP, Net primary productivity (NPP) and evapotranspiration (ET). Key features of BEPS include the incorporation of sunlit-shaded leaf stratification strategy (Norman, 1982). The model calculates canopy-level photosynthesis by summing the GPP of sunlit and shaded leaves (Chen et al., 1999).

$$GPP = A_{sun}LAI_{sun} + A_{shade}LAI_{shade} \quad (1)$$

$$LAI_{sun} = 2\cos\theta\left[1 - exp\left(-\frac{0.5\Omega LAI}{\cos\theta}\right)\right] \quad (2)$$

$$LAI_{shade} = 1 - LAI_{sun} \quad (3)$$

where A_{sun} and A_{shade} represent the amount of photosynthesis at per sunlit and shaded leaf, respectively; LAI_{sun} and LAI_{shade} represent the canopy-level sunlit and shaded LAI, respectively; Ω is the foliage clumping index indicaiting the influence of foliage clustering on radiation transmission, and θ is the solar zenith angle.

The accuracy of carbon flux products simulated by BEPS has been validated in previous studies (Chen et al., 2019; He et al., 2021). We also used the measured site data from ChinaFlux (http://chinaflux.org/) and National Tibetan Plateau Third Pole Environment (Li et al., 2013) (Table S1) to assess the performance of BEPS simulated GPP (Fig. S1). Our analysis reveals a high consistency between simulated and observed GPP, with an average R^2 of 0.77 ($p < 0.05$) and an average root mean square error (RMSE) of 1.70 gC m^{-2} day^{-1}. In addition, the global terrestrial GPP from FluxSat product Version 2.2 (Joiner et al., 2018) was also used to assess

the reliability of BEPS GPP. FluxSat GPP is obtained by using light-use efficiency (LUE) framework based on Moderate-resolution Imaging Spectroradiometer (MODIS) satellite data, eliminating the dependency on other meteorological input data. The comparison between BEPS GPP and FluxSat GPP data revealed a robust agreement, with a correlation coefficient (r) of 0.63 ($p < 0.05$) and a RMSE of 1.1 Pg C yr^{-1} (Fig. S2). These consistencies underscore the reliability of the BEPS GPP data in capturing terrestrial carbon flux dynamics.

2.2 Anomaly calculation

To calculate anomalies, we initially eliminated the long-term climatology to get rid of the seasonal cycle. Subsequently, we subtracted the 7-year running average for each grid to eliminate the decadal oscillation and long-term trends for all the variables. Further, refinement involved smoothing the derived GPP and climate anomalies using a 3-month running average to remove the intra-seasonal variability. For consistency, the BEPS simulated GPP data was resampled to 0.1° × 0.1°. To align with this, non-vegetated areas in the climate data were masked according to the resampled BEPS GPP, uniformity in spatial representation.

2.3 Definition of climate events

The Oceanic Niño Index (ONI) is used to define ENSO events (Fig. 1a), which represents the 3-month running mean SST anomaly in the Niño 3.4 region (5°N-5°S, 120°-170°W). The positive phase of an ENSO event (El Niño) is characterized by the ONI exceeding +0.5K for five consecutive overlapping 3-month periods. Conversely, the negative phase of an ENSO event (La Niña) occurs when the ONI is below −0.5K for five consecutive overlapping 3-month periods. The severity of the event can be further categorized into weak (0.5~–0.99), moderate (1.00~–1.49), strong (1.50~–1.99) and extremely strong (⩾2.00) based on the absolute value of the ONI. To qualify for a specific rating, an event should meet or exceed a threshold for at least three consecutive overlapping three-month periods.

Moreover, the Dipole Mode Index (DMI) is employed to identify IOD events (Saji et al., 1999). The DMI is calculated from SST differences between the Western Equatorial Indian Ocean (10°S-10°N, 50°-70°E) and the South-eastern Equatorial Indian Ocean (10°S-0°N, 90°-110°E) (Fig.1b). Given that the short duration of IOD events with a tendency to peak during the SON, the standard deviation of SON DMI (0.52K from 1981 to 2021) is used as the criterion for identifying IOD events. A positive phase IOD (pIOD) event is defined when the absolute value of DMI is greater than or equal to one standard deviation (0.52 K) for three consecutive 3-month periods. Additionally, a strong pIOD event is identified if the DMI value exceeds two standard deviations (1.04 K).

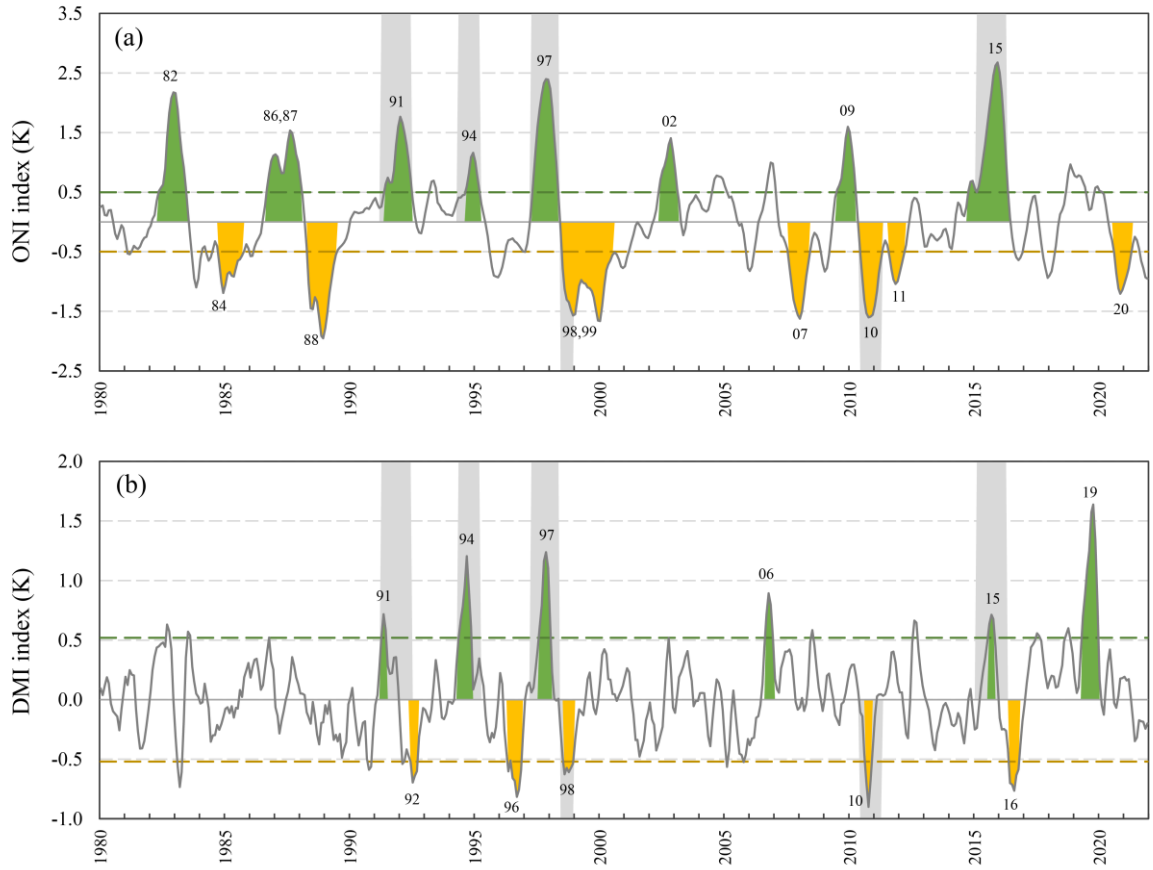

Fig.1 Time series of the Oceanic Niño Index (ONI) (a) and the Dipole Mode Index (DMI) (b) from 1980 to 2022. The positive phase events (El Niño and positive Indian Ocean Dipole (pIOD)) are filled in green and the negative phase events (La Niña and negative IOD (nIOD)) are filled in yellow, and the events are also labeled with a two-digit year. The green and yellow dashed lines represent the positive and negative thresholds for El Niño-Southern Oscillation (ENSO) and IOD, respectively. The gray

background indicates years with the simultaneous ENSO and IOD events.

2.4 Partial correlation analysis

To comprehensively assess the impacts of ENSO and IOD on GPP, while accounting for the influence of other events, partial correlation analysis (pcor) was employed, following the previous studies (Saji and Yamagata, 2003; Wang et al., 2021b). The definition of *pcor* for *x* and *y*, controlling for *z*, is given by:

$$pcor_{yx.z} = \frac{r_{yx} - r_{yz}r_{xz}}{\sqrt{1-r_{yz}^2}\sqrt{1-r_{xz}^2}} \quad (4)$$

where r_{yx} is the correlation of the dependent variable *y* and the explanatory variable *x* (e.g., DMI), and the same is for r_{yz} and r_{yx}. The two-tailed Student's *t*-test was used to calculate the statistical significance of each pixel result:

$$t = pcor_{yx.z}\sqrt{\frac{n-2-k}{1-pcor_{yx.z}^2}} \quad (5)$$

where *n* and *k* are the number of samples and conditioned variables, respectively.

2.5 Composite analysis

When enumerating the years of ENSO and IOD events, we retained all the years of IOD events and ENSO events of above the moderate intensity. Individual events and compound events were categorized and summarized in Table 1. In this study, a compound event refers to the simultaneous occurrence of ENSO and IOD, primarily El Niño & pIOD and La Niña & negative IOD (nIOD). IOD typically peaked in the September-October-November (SON, yr0), while ENSO peaked in the December(yr0)-January(yr1)-February(yr1) (DJF), and the influence of the two events could extend until the summer of the following year. Therefore, we selected four seasons from SON to June-July-August (JJA) in the following year for composite analysis in this study. In addition, the year 1991 was excluded due to the strong eruption of Mount Pinatubo, which had a large impact on the global carbon cycle (Mercado et al., 2009).

220 **Table 1**. Occurrences of ENSO and IOD events from 1981 to 2021.

Events	Years
El Niño	1982, 1986, 1987, 2002, 2009
La Niña	1984, 1988, 1999, 2007, 2011, 2020
pIOD	2019
nIOD	1992, 1996, 2016
El Niño & pIOD	1994,1997, 2015
El Niño & nIOD	-
La Niña & pIOD	-
La Niña & nIOD	1998, 2010

221

3.Results

3.1 Historical relationship between GPP and ENSO

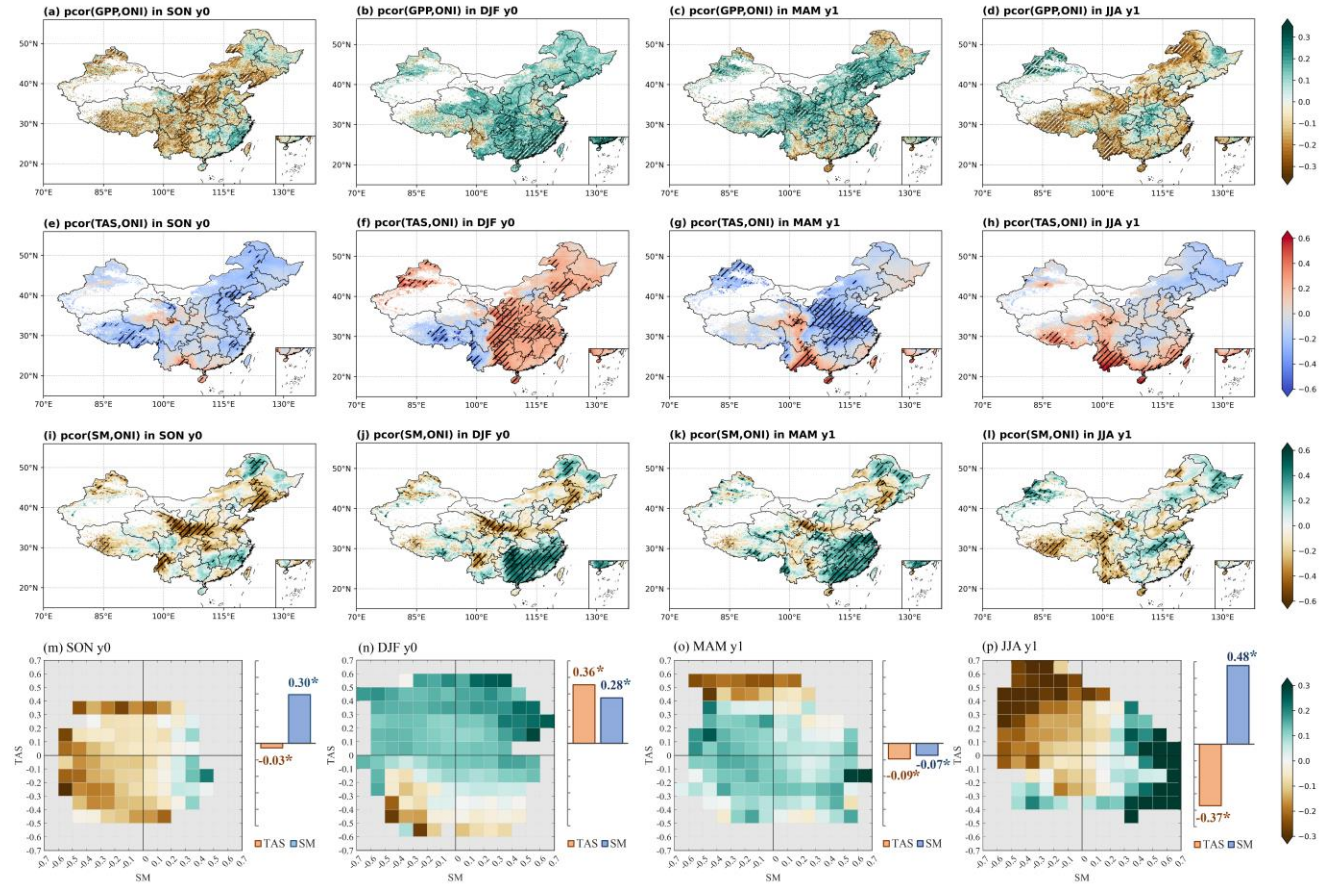
(a) pcor(GPP,ONI) in SON y0
(b) pcor(GPP,ONI) in DJF y0
(c) pcor(GPP,ONI) in MAM y1
(d) pcor(GPP,ONI) in JJA y1
(e) pcor(TAS,ONI) in SON y0
(f) pcor(TAS,ONI) in DJF y0
(g) pcor(TAS,ONI) in MAM y1
(h) pcor(TAS,ONI) in JJA y1
(i) pcor(SM,ONI) in SON y0
(j) pcor(SM,ONI) in DJF y0
(k) pcor(SM,ONI) in MAM y1
(l) pcor(SM,ONI) in JJA y1
(m) SON y0
(n) DJF y0
(o) MAM y1
(p) JJA y1
0.30*
-0.03*
0.36*
0.28*
-0.09*
-0.07*
0.48*
-0.37*
TAS
SM

224

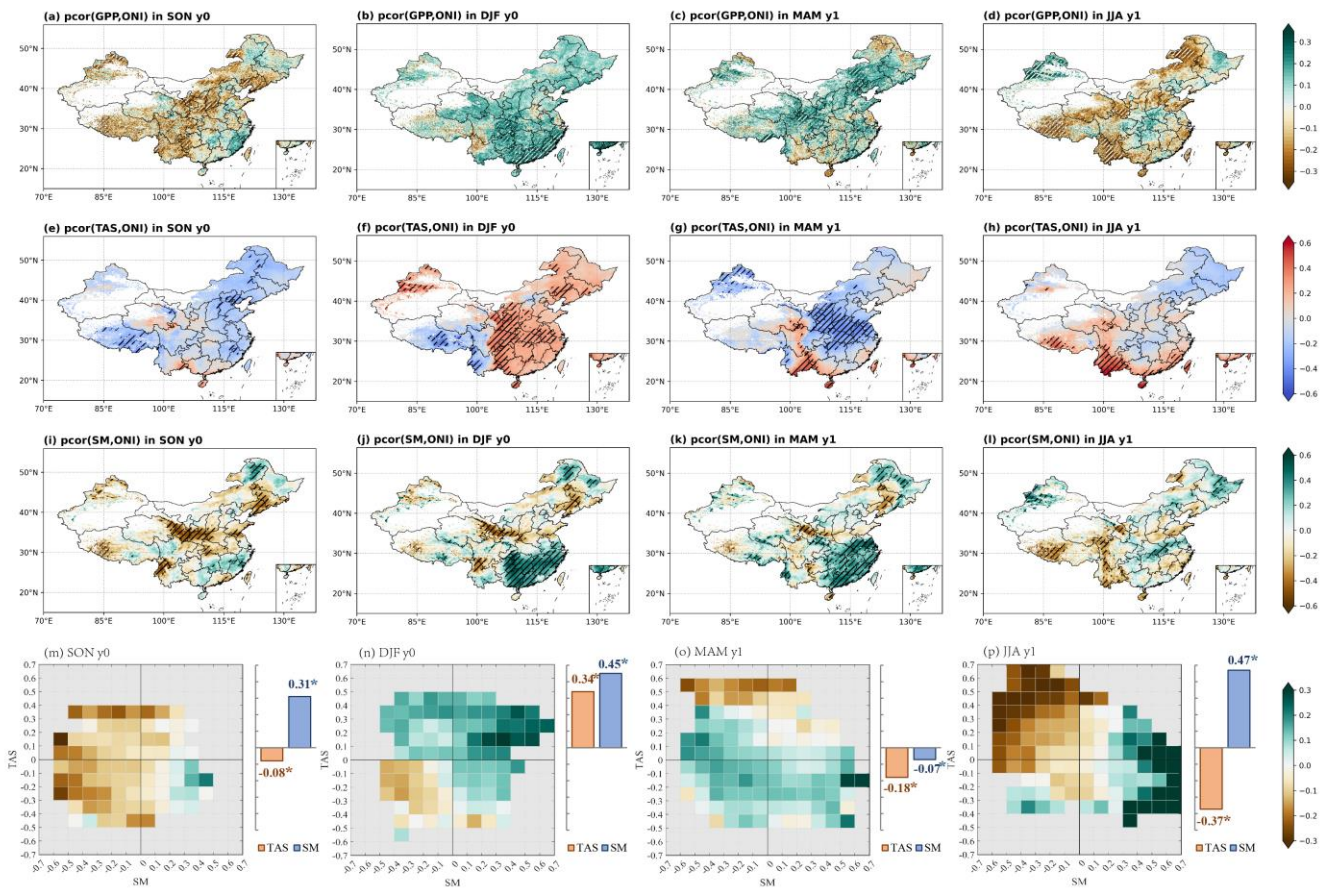
(a) pcor(GPP,ONI) in SON y0
(b) pcor(GPP,ONI) in DJF y0
(c) pcor(GPP,ONI) in MAM y1
(d) pcor(GPP,ONI) in JJA y1
(e) pcor(TAS,ONI) in SON y0
(f) pcor(TAS,ONI) in DJF y0
(g) pcor(TAS,ONI) in MAM y1
(h) pcor(TAS,ONI) in JJA y1
(i) pcor(SM,ONI) in SON y0
(j) pcor(SM,ONI) in DJF y0
(k) pcor(SM,ONI) in MAM y1
(l) pcor(SM,ONI) in JJA y1
(m) SON y0
(n) DJF y0
(o) MAM y1
(p) JJA y1
0.31*
-0.08*
0.45*
0.34*
-0.18*
-0.07*
0.47*
-0.37*
TAS
SM

225

Fig. 2 Spatial patterns of partial correlation coefficients (*pcor*) between ONI and gross primary productivity (GPP) (a-d), surface air temperature (TAS) (e-h), soil moisture (SM) (i-l) in different seasons, controlling for the effect of DMI. Hatched areas represent significance at $p \leq 0.05$ based on the two-tailed Student's *t*-test. (m-p) Heatmaps represent the relationships of the *pcor* patterns among GPP, TAS, and SM, and bar charts illustrate the pattern correlations of these *pcor* values between GPP and TAS and SM on the national scale for each season. We here use seasonal average temperature as a mask to exclude regions with temperatures below zero, thereby minimizing the influence of phenology on GPP. Notably, asterisks (*) in the bar charts denote significance at $p < 0.05$.

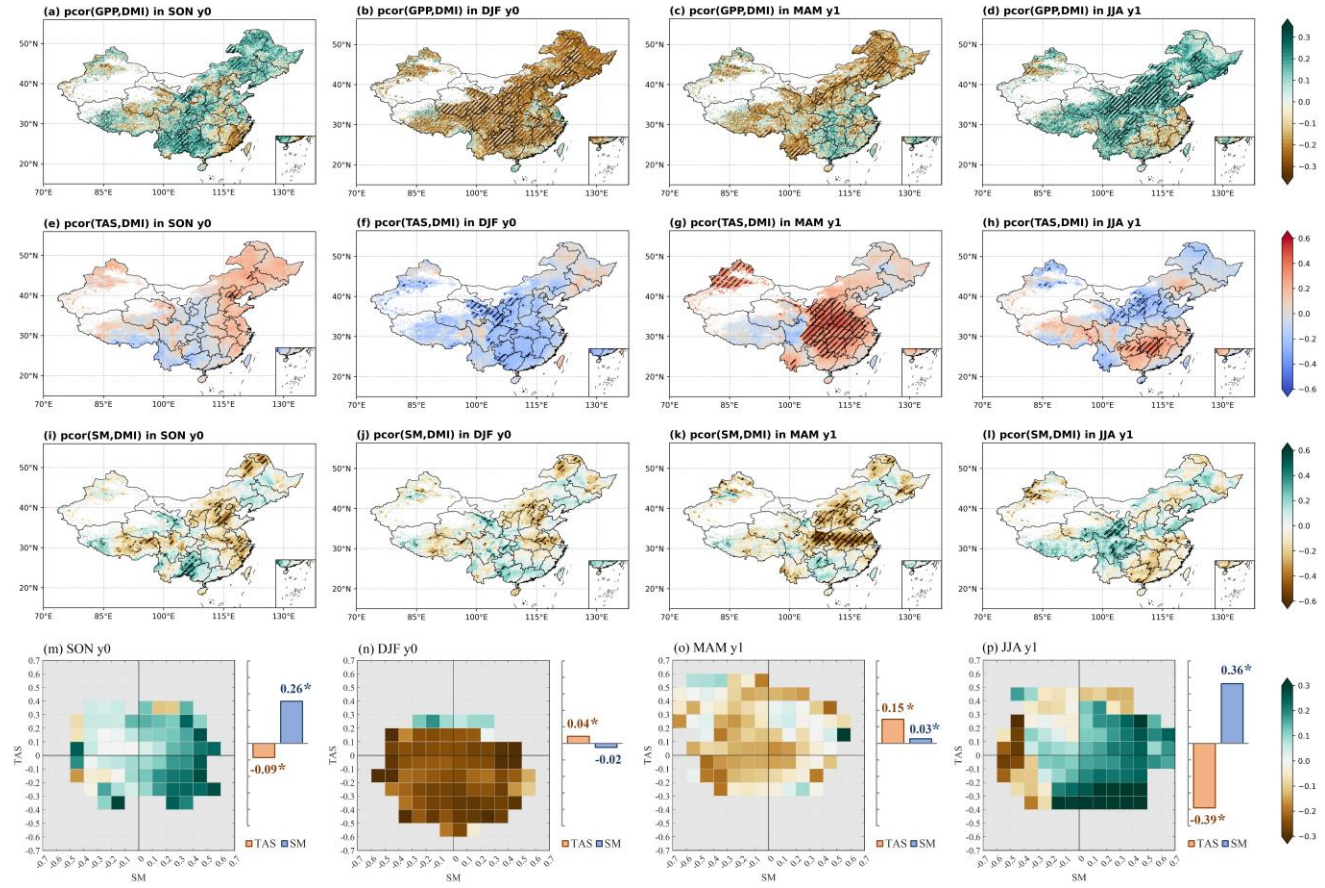
(a) pcor(GPP,DMI) in SON y0
(b) pcor(GPP,DMI) in DJF y0
(c) pcor(GPP,DMI) in MAM y1
(d) pcor(GPP,DMI) in JJA y1
(e) pcor(TAS,DMI) in SON y0
(f) pcor(TAS,DMI) in DJF y0
(g) pcor(TAS,DMI) in MAM y1
(h) pcor(TAS,DMI) in JJA y1
(i) pcor(SM,DMI) in SON y0
(j) pcor(SM,DMI) in DJF y0
(k) pcor(SM,DMI) in MAM y1
(l) pcor(SM,DMI) in JJA y1
(m) SON y0
0.26*
-0.09*
(n) DJF y0
0.04*
-0.02
(o) MAM y1
0.15*
0.03*
(p) JJA y1
0.36*
-0.39*
TAS
SM

234

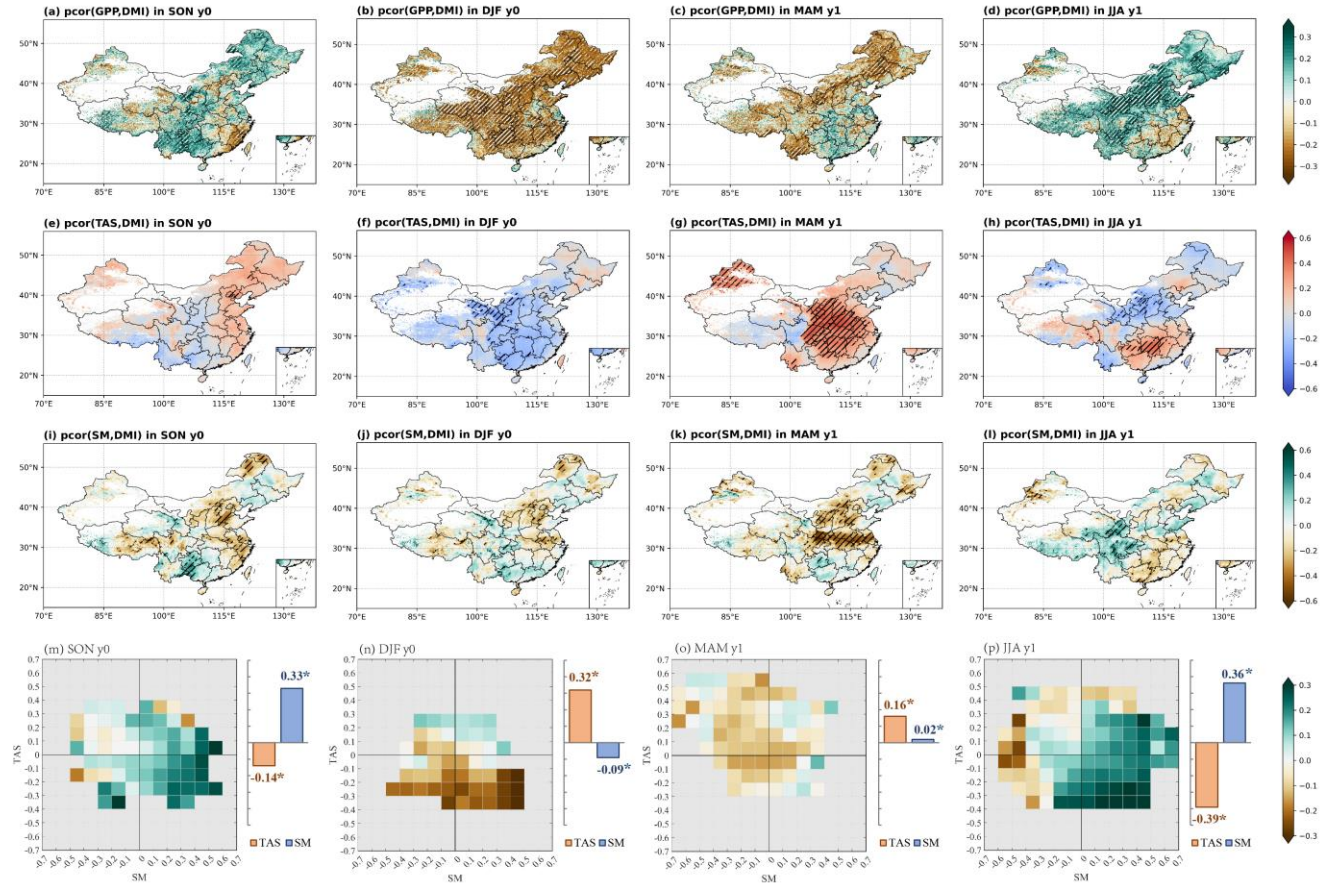
(a) pcor(GPP,DMI) in SON y0
(b) pcor(GPP,DMI) in DJF y0
(c) pcor(GPP,DMI) in MAM y1
(d) pcor(GPP,DMI) in JJA y1
(e) pcor(TAS,DMI) in SON y0
(f) pcor(TAS,DMI) in DJF y0
(g) pcor(TAS,DMI) in MAM y1
(h) pcor(TAS,DMI) in JJA y1
(i) pcor(SM,DMI) in SON y0
(j) pcor(SM,DMI) in DJF y0
(k) pcor(SM,DMI) in MAM y1
(l) pcor(SM,DMI) in JJA y1
(m) SON y0
0.33*
-0.14*
(n) DJF y0
0.32*
-0.09*
(o) MAM y1
0.16*
0.02*
(p) JJA y1
0.36*
-0.39*
TAS
SM

235

Fig. 3 Same as Fig.2, but for DMI, controlling the effect of ONI.

We analyzed the *pcor* patterns between GPP and ~~,~~ climate anomalies~~, and~~ across different events using long time series data (Figs. 2 and 3). Following this, we calculated pattern correlation coefficients between the GPP and climate *pcor* patterns ~~(including all the pixels over China)~~, aiming to investigate the varying impacts of key climate drivers (TAS and SM) on photosynthesis across different seasons (Figs. 2m-p, and 3m-p).

Figure 2 reveals notable seasonal variations in the *pcor* patterns between GPP, related climate anomalies, and ONI index in December-January-February (DJF) when ENSO peaked, controlling the effect of DMI in September-October-November (SON) when IOD peaked. During SON, significant negative *pcor* between GPP and ONI is observed in regions including the Tibetan Plateau, Southwestern China, Loess Plateau, and Liaoning province (Fig. 2a). Clearly, this pattern aligns closely with the *pcor* pattern between soil moisture and ONI (Figs. 2a and i). The pattern correlation analysis between GPP and both TAS and SM underscores the dominance of SM in influencing GPP anomalies, indicated by a correlation coefficient of 0.31~~30~~ ($p < 0.05$). This finding suggests that the soil moisture deficit induced by El Niño largely inhibits vegetation photosynthesis during this season (Fig. 2m).

Along with the peak of ENSO events in DJF, the *pcor* pattern between GPP and ONI exhibits a distinct shift from the pattern in SON. Notably, DJF showcases significant positive *pcor* values over large areas in southern China and weak positive *pcor* in the North and Northeastern China (Fig. 2b). During this period, ~~temperature~~soil moisture still ~~emerges~~ serves as a more influential factor in driving GPP changes, reflected in a nation-wide pattern correlation coefficient of 0.~~32~~45 ($p < 0.05$) (Fig. 2n). Specifically, sufficient soil moisture ~~higher winter temperatures~~ during El Niño, coupled with higher winter temperatures~~sufficient soil moisture~~, contribute to a substantial enhancement in GPP across Southern China. In contrast, the impact is weaker in the North and Northeast China due to the vegetation being in the non-growing season, and localized soil water deficits (Figs. 2b, f, and j). In addition, GPP experiences

inhibition in some areas of southwestern China due to low temperatures and soil drought.

Subsequently, the positive *pcor* of GPP decreases, or even turns ~~into weak~~ slightly negative ~~values~~ from DJF to March-April-May (MAM) in southern China~~.~~, ~~which These changes are~~ primarily attributed to shifts of temperature~~, with a pattern correlation coefficient of −0.09 (p < 0.05)~~ (Figs. 2c~~,~~ and g~~, and o~~). On a nationwide scale, ~~Conversely, the positive *pcor* of GPP continues to increase in northern Sichuan, aligning with the positive *pcor* of temperature (Figs. 2c and g), and in northern Hebei and parts of neighboring Inner Mongolia, corresponding to the weak positive *pcor* of soil moisture (Figs. 2c and k).~~ temperature becomes the dominant factor in this period, but it exhibits a negative correlation with GPP, with a spatial correlation coefficient of −0.18 (p < 0.5). This negative correlation is mainly due to negative GPP and positive temperature in the southwest region, and positive GPP and negative temperature in the northern region (Figs. 2c and 2g). Specifically, the negative *pcor* of GPP in southwest China is due to soil moisture shortages (Fig. 2k). In the northern region, where a large area of croplands exists (Fig. S11), human management practices may have a greater impact on GPP, particularly in the spring when the growing season begins. However, these human management practices (e.g., irrigation, fertilization, pesticide use) are not considered in the BEPS model, which could introduce significant uncertainties in simulated GPP over cropland areas. Additionally, in some grasslands of northern Hebei and parts of neighboring Inner Mongolia, GPP shows positive *pcor* during El Niño events, possibly due to the strong legacy effects of climatic conditions in DJF period.

Moving into JJA, the *pcor* of GPP exhibits widespread negative values again (Fig. 2d). In general, during El Niño, increased soil moisture and lower temperatures greatly contribute to enhanced GPP, while drier soil moisture and higher temperatures inhibit the increase in GPP (Fig. 2p). Regionally, higher temperatures and lower soil moisture both contribute to the negative GPP anomalies over southwestern China. However, lower soil moisture predominantly curtails GPP over the Tibetan Plateau, the Yellow River basin, and northeastern

Inner Mongolia. Overall, the correlation coefficients between GPP and TAS and SM in summer are comparable, with soil moisture exhibiting a slightly higher effect, represented by a correlation coefficient of ~~=~~0.47~~39~~ ($p < 0.05$), compared to a correlation coefficient of −0.37~~0.36~~ ($p < 0.05$) for temperature~~ soil moisture~~.

3.2 Historical relationship between GPP and IOD

In comparison, the *pcor* patterns between GPP and DMI in SON, controlling for the effect of ONI~~ in DJF~~, exhibit nearly opposite patterns to those between GPP and ONI (Figs. 2 and 3). In detail, GPP demonstrates significant positive *pcor* values with DMI in southwestern China and eastern Inner Mongolia, but displays significant negative *pcor* with DMI in southeastern China during SON (Fig. 3a). In terms of climate drivers, during the pIOD events, for instance, wetter soil and lower temperatures both benefit the significant enhancement in GPP in southwestern China, while higher temperatures largely contribute to the enhancement in GPP over eastern Inner Mongolia. Conversely, GPP is largely inhibited by the dry conditions in southeastern China (Figs. 3e and i). Overall, soil moisture dominates the GPP anomaly in China, with a correlation coefficient of 0.33~~26~~ ($p < 0.05$) (Fig. 3m).

In DJF, GPP exhibits widespread significant negative *pcor* with DMI (Fig. 3b), primarily due to the widespread negative *pcor* of temperature, characterized by a correlation coefficient of 0.32~~04~~ ($p < 0.05$) (Figs. 3f and n). Moving into MAM, the significant negative *pcor* between GPP and DMI carried on from those in DJF, but shifts to weak positive *pcor* in southeastern China, driven by the significant positive *pcor* of temperature (Figs. 3c and g). However, the significant negative *pcor* of soil moisture in the Jianghuai Basin and North China still negates the positive effect of temperature (Fig. 3k). During this period, temperature remains the dominant factor, with a nation-wide pattern correlation coefficient of 0.~~15~~ 16 ($p < 0.05$) with GPP (Fig. 3o).

In JJA, the situation undergoes a change, showing the significant positive *pcor* of GPP over southwestern, north and northeast China, and weak negative *pcor* over southeastern China (Fig. 3d). In other words, lower temperatures and gradually wetter soil are conducive to the increase in vegetation photosynthesis, but heat and dry conditions cause the weak inhibition of photosynthesis in southeastern China during the pIOD (Figs. 3p). However, unlike the ENSO event, the role of temperature is slightly higher than that of SM in the IOD event, and the correlations between GPP and TAS and SM are −0.39 and 0.36 ($p < 0.05$), respectively.

3.3 GPP anomalies caused by specific ENSO and IOD events

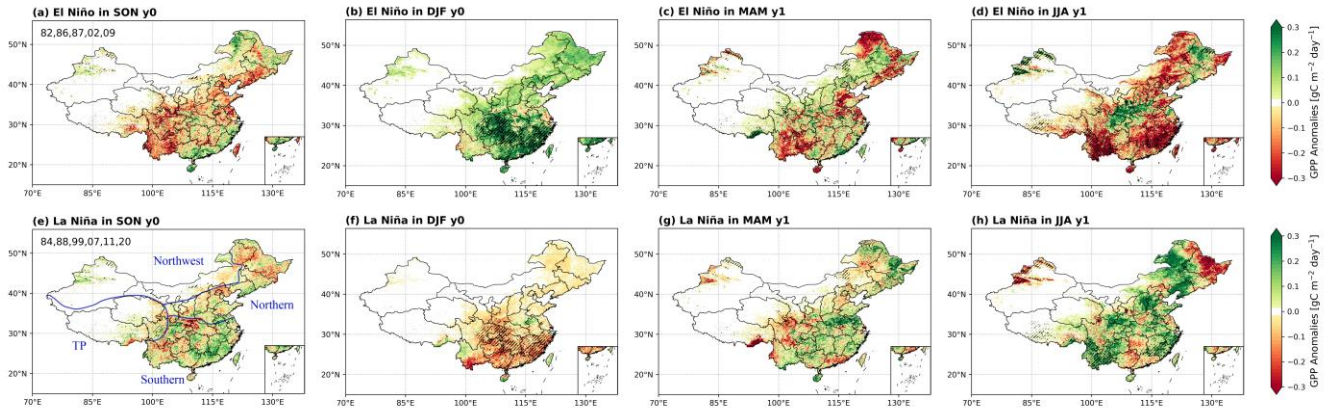

Fig. 4. Spatial distributions of seasonal composite GPP anomalies for ENSO events, (a-d) for El Niño, and (e-h) for La Niña. The black slashes indicate areas where El Niño events differ significantly from La Niña events ($p \leq 0.05$) based on the Student's two-sample *t*-test. The two-digit year in first column denote the years used for composite analysis. Additionally, China is divided into four regions: Northwest China, Tibetan Plateau, Northern China, and Southern China, as shown in (e), which is used in the following context.

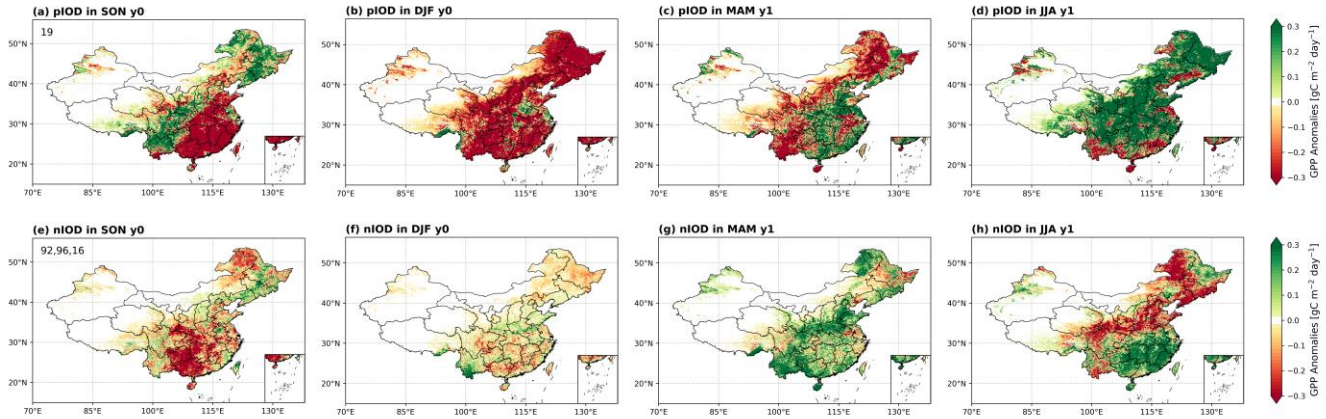

Fig. 5. Similar to Fig. 4, but for spatial distributions of seasonal composite GPP anomalies for IOD events, (a-d) for pIOD, and (e-h) for nIOD. We did not conduct the significance test here owing to the limited samples.

While we have elucidated the historical relationship between GPP and ENSO and IOD events through partial correlation coefficients and discussed the underlying climate drivers, we here specifically selected actual events to conduct a composite analysis. This approach aims to further comprehensive understanding of the effects of ENSO and IOD events on GPP variations in China.

3.3.1 ENSO-induced GPP anomalous patterns

The impacts of El Niño and La Niña events exhibit opposite influences on GPP with obvious seasonal variations (Fig. 4). Specifically, during SON, GPP anomalies are relatively weak, indicating some suppressions over southwestern China and north China during El Niño events, primarily attributed to dry conditions there (Figs. 4a and S4a). As ENSO peaks in DJF, GPP is significantly strengthened during El Niño events and suppressed during La Niña events, especially over southern China (Figs. 4b and f), aligning well with the patterns of *pcor* between GPP and ONI, controlling the effect of DMI (Fig. 2b). Concurrently, the widespread higher temperatures and wetter soil moisture both contribute to enhanced GPP over southern China during El Niño events (Figs. S3b and S4b), while colder temperatures and drier soil moisture lead to GPP suppression there during La Niña (Figs. 2f and 3f). In MAM as ENSO weakens and vegetation starts to grow in the extratropics, the enhanced GPP over southern China in DJF during El Niño events diminishes, even transitioning into a notable GPP reduction over southwestern China, north China, and northeastern China (Fig. 4c). This transition is conspired by phenological and climate changes including colder temperatures and prolonged dry conditions (Figs. S3c and S4c). The GPP pattern exhibits the opposite transition in La Niña (Fig. 4g). Moving to JJA, dry and hot conditions (Fig. S3d and S4d) lead to significant negative GPP anomalies in southeastern and southwestern China in El Niño (Fig. 4d), whereas cool and wet conditions result in positive GPP anomalies in La Niña events (Fig. 4h). Overall, GPP anomalies induced by ENSO events in DJF and JJA are more pronounced than those in SON and MAM, corresponding to the life cycle of event and vegetation growth periods, respectively.

Crucially, they demonstrate distinct GPP patterns, with significant enhancements in DJF and reductions in JJA during El Niño events and reverse during La Niña events, aligning well with the *pcor* pattern between GPP and ONI, controlling for the effect of DMI (Fig. 4). In addition, the effect of ENSO on vegetation in southern China appears more substantial.

3.3.2 IOD-induced GPP anomalous patterns

During the period from 1981 to 2021, we only find one independent but extreme pIOD event occurred in 2019 according to our criterion (Table 1). This extreme pIOD event extended from June to December, a longer duration compared to other IOD events. Different from ENSO, IOD basically peaks in SON. GPP anomalies induced by this extreme event align closely with the long-term *pcor* patterns between GPP and DMI, controlling for the effect of ONI (Fig. 3). Specifically, significant reductions in GPP occur in southeastern China in SON (Fig. 5a), predominantly due to heat stress and severe drought conditions (Figs. S5a and S6a), consistent with the findings revealed by Wang et al. (2021b). In DJF, the seasonal legacy of vegetation state (Yan et al., 2023) and prolonged droughts lead to the widespread GPP reductions (Figs. 5b and S6b), outweighing the potential positive effect of higher temperatures (Fig. S5b). Of course, the decline of GPP in southwestern China appears linked to lower temperatures (Figs. 5b and S5b). During MAM, the mitigation of soil moisture deficit and favorable higher temperatures in southern China facilitate a shift in GPP from decline to increase (Fig. 5c). In the north, persistent drought conditions notwithstanding (Fig. S6c), higher temperatures and the onset of the growing season contribute to the enhanced GPP (Fig. 5c). In JJA, increased precipitation over the Yangtze and Yellow River basins (*Zhang et al.*, 2022) alleviates the soil moisture deficits (Fig. S6d). Coupled with the relatively lower temperatures, this leads to widespread GPP increases. Conversely, GPP suppressions in provinces south of 25°N and around the Bohai Sea are attributed to higher temperatures and soil water deficits (Figs. 5d, S5d, and S6d).

In contrast to the intense 2019 pIOD event, our composite analysis incorporates three weak nIOD events, resulting in comparatively milder anomalies. In SON, different from pIOD event, negative GPP anomalies in nIOD mainly appear in the provinces of Guizhou, Hunan, and Guangxi (Fig. 5e), associated well with concurrent dry conditions (Fig. S6e). In DJF, although the spatial pattern of soil moisture remains largely consistent with SON (Fig. S6f), a shift from negative to positive temperature anomalies mitigates the evident GPP reductions (Fig. 5f). The ongoing soil wetting and the onset of the growing season in northern hemisphere in MAM result in the increased GPP over the Yellow River Basin and southwestern China (Figs. 5g, S5g, and S6g). Subsequently, in JJA, the combination of wetter soil and lower temperatures facilitates vegetation photosynthesis in southern China, while drier soil largely contributes to the reduction in GPP in the north and northeastern China (Figs. 5h, S5h, and S6h).

3.3.3 National and regional total GPP anomalies

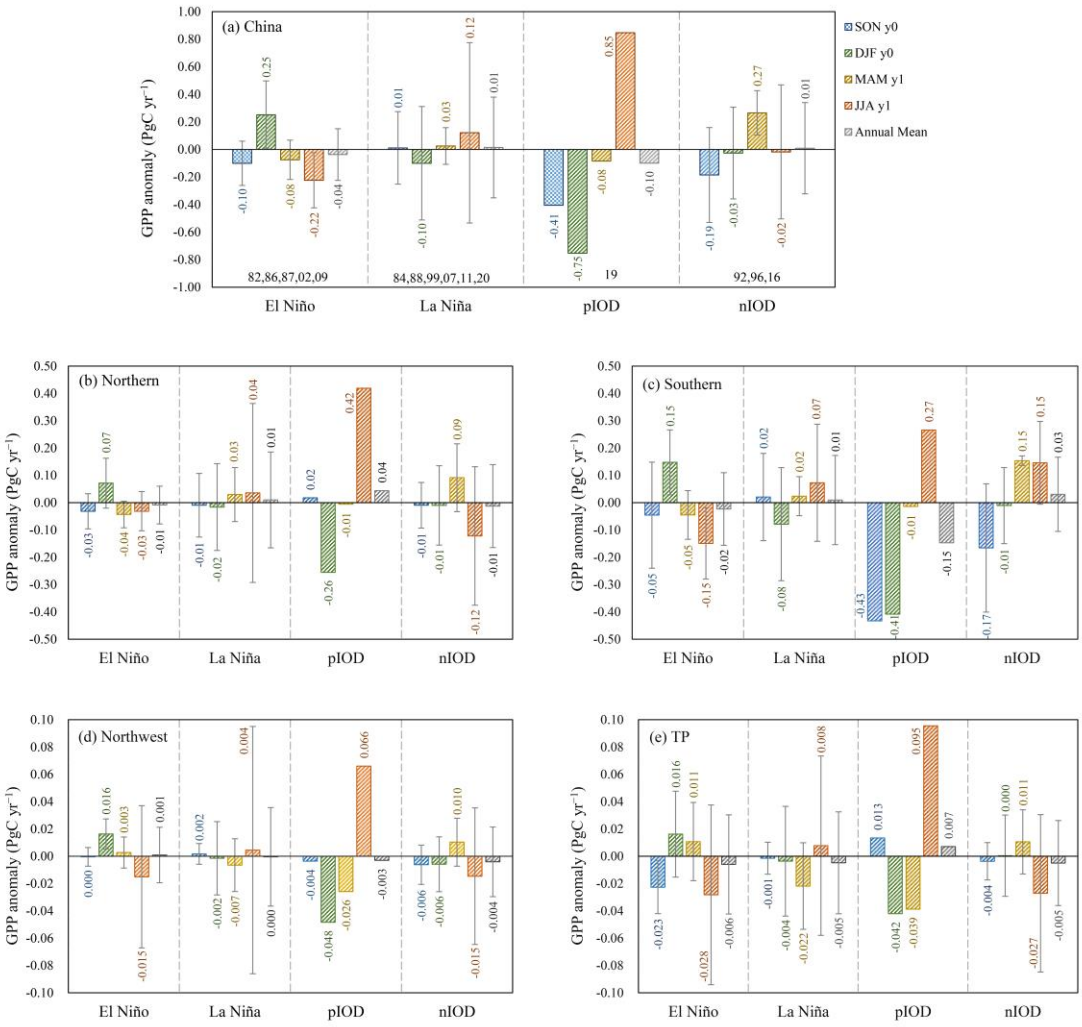

Fig. 6. The seasonal and annual mean anomaly of GPP in different classified events for China (a), for Northern China (b), for Southern China (c), for Northwest China (d), and for Tibetan Plateau (e). The error bars show the standard deviation of different events in the composite analysis.

We calculated the total GPP anomaly in China and various geographic regions for each classified event on both seasonal and annual scales (Fig. 6). Regionally, the geographical divisions include Northern China, Southern China, Northwest China, and Tibetan Plateau (Fig. 4e). Notably, the North-South boundary aligns closely with the 0° isotherm in January and the annual precipitation line of 800 mm. The division between the North and the Northwest is

419 determined by the annual precipitation line of 400 mm, and the Tibetan Plateau is segmented
420 based on topographic factors.
421
422 In general, the GPP anomalies exhibit noticeable differences on the seasonal scale, while the
423 total annual anomalies do not show a significant magnitude due to the mutual offset of positive
424 and negative anomalies in different seasons. However, it is worth noting that our annual totals
425 are calculated from the SON in the developing year of the event to the JJA in the following
426 year. This method deviates from the traditional calendar year, and as per the conventional
427 definition of a "year", the annual anomalies induced by these events can indeed be substantial.
428
429 Specifically, taking a national perspective (Fig. 6a), GPP anomalies during the El Niño and La
430 Niña events exhibit opposite signs in DJF and JJA, with greater magnitudes during these peak
431 periods of the events and the most vigorous growth period of vegetation, respectively. In terms
432 of the development process of the event, the annual anomaly of GPP is negative during El Niño,
433 with a magnitude of -0.04 ± 0.19 Pg C yr^{-1}, but positive during La Niña events, with a
434 magnitude of 0.01 ± 0.37 Pg C yr^{-1}. The asymmetry of the positive and negative phases of IOD
435 is also evident in the total anomaly. For the pIOD event in 2019, GPP shows strong negative
436 anomalies with values of -0.41 Pg C yr^{-1} in SON and -0.75 Pg C yr^{-1} in DJF. Conversely, it
437 exhibits a marked positive anomaly in the following JJA, with a value of 0.85 Pg C yr^{-1}. The
438 annual total of GPP anomaly is opposite for pIOD and nIOD events, showing -0.10 Pg C yr^{-1}
439 and 0.01 ± 0.33 Pg C yr^{-1}, respectively. Moreover, large standard deviation indicated that there
440 are large uncertainties in the impact of different events, and each event has its uniqueness
441 (Capotondi et al., 2015).
442
443 Additionally, the variation of GPP anomaly in each region is basically consistent with that at
444 the national scale, especially in the Southern. But regional differences indeed exist in the total
445 amount of GPP anomalies, demonstrating the difference in the impact of events on different
446 regions' GPP. Taking the 2019 extreme pIOD event as an example, the GPP showed a

447 significant negative anomaly in the Southern during the SON (Fig. 6c), resulting in negative
448 anomalies in GPP at the national scale (Fig. 6a), but weak positive anomalies in the Northern
449 and TP (Figs. 6b and e). Then, the GPP anomaly was close to zero in the Northern and Southern
450 in MAM (Figs. 6b and c), while it was still a significant negative anomaly in the Northwest
451 and TP (Figs. 6d and e). Moreover, the negative annual GPP anomalies in the Southern and
452 Northwest offset the positive anomalies of the TP and Northern, making a negative annual GPP
453 anomaly in the national of this event.
454
455 In terms of the magnitude of GPP anomalies, they are more pronounced in the Northern and
456 Southern regions, characterized by lusher vegetation, mostly less than 0.5 Pg C yr^{-1}.
457 Meanwhile, GPP anomalies are relatively weaker in the Northwest and TP regions, primarily
458 covered by grassland, generally less than 0.1 Pg C yr^{-1}. Further, we calculate the contributions
459 of different regions to the national total GPP anomaly in each event (Table S3), referencing an
460 index described in the article by Ahlstrom et al. (2015), as detailed in the supplementary method.
461 Overall, the GPP anomaly in the Southern region dominates the national GPP variation,
462 contributing approximately 68% to ENSO events and 46% to IOD events, respectively. The
463 Northern GPP anomaly contributes approximately 28% to the national GPP variation in ENSO
464 events and 39% in IOD events. In addition, the contribution of GPP anomaly in the Northwest
465 and TP regions to the national GPP variation is within 10%.

3.3.4 Relative changes in total GPP anomalies at provincial scale

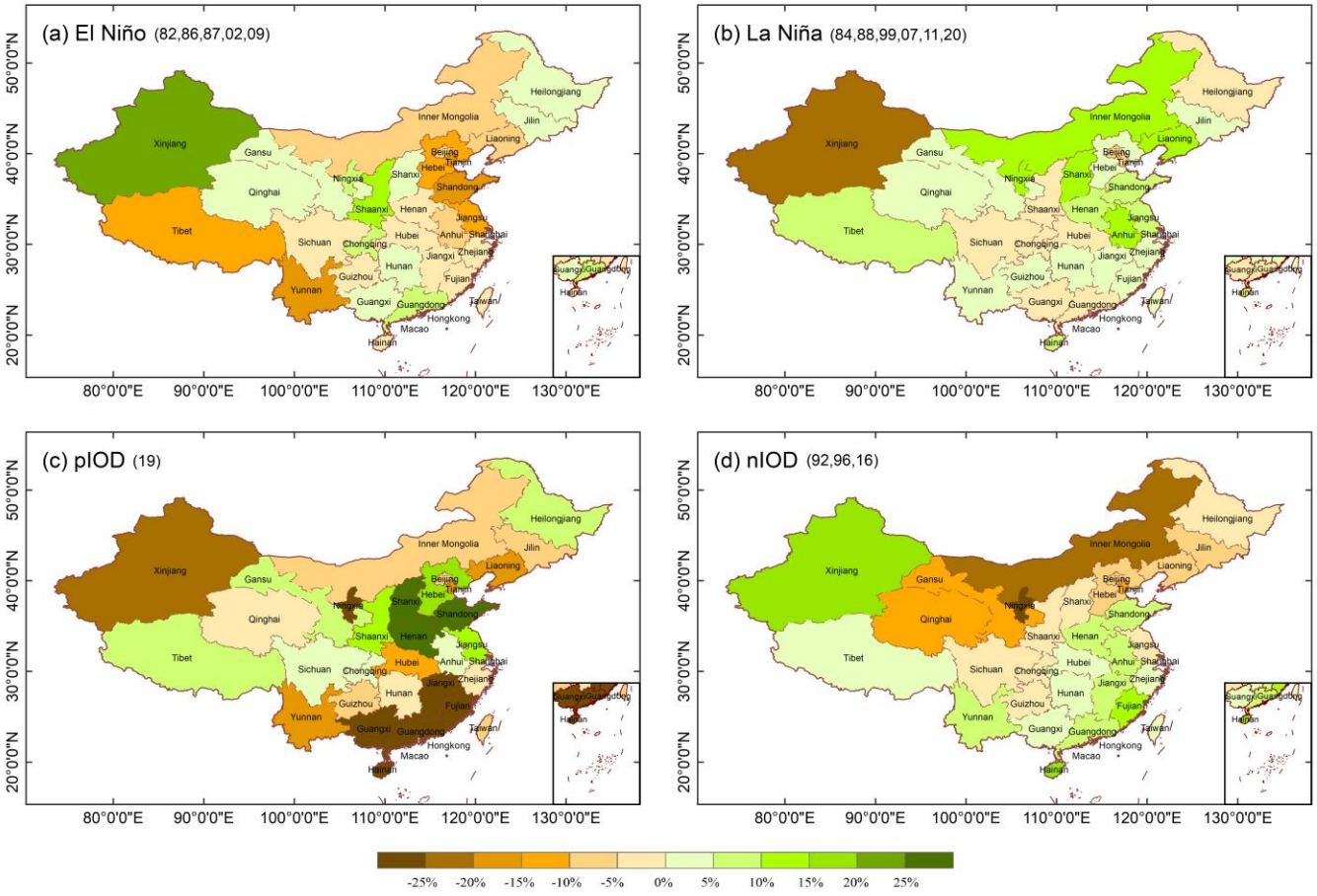

Fig. 7. Spatial distributions of relative changes of total composite anomalies of GPP at provincial scale for different classified events.

We presented the spatial patterns of mean GPP anomalies from the SON in the developing year to the JJA in the decaying year (Fig. S7) and further calculated provincial total GPP anomalies (Fig. S8 and Table S3). Provinces with more extensive forest coverage, such as Yunnan, central provinces housing the Qinling Mountains, and northeast provinces where the Greater and Lesser Hinggan Mountains are situate, exhibit relatively larger provincial GPP anomalies. However, differences are apparent among different events (Fig. S8). Considering differences in area and vegetation coverage across provinces, our focus centers on the relative change of GPP anomalies (Fig. 7). It's important to note that, due to different years used in composite analysis, our quantitative comparisons are limited to the same event within different provinces, while qualitative descriptions are extended to different events.

El Niño events generally induce substantial GPP changes in two main regions with a relative change of over 10% (Fig. 7a). One region encompasses the northern coastal provinces, including Tianjin, Hebei, Shandong, and Jiangsu, while the other is situated in the western part, including Xinjiang, Tibet, and Yunnan provinces. Yunnan, rich in forest resources, bears the brunt of El Niño 's impact, exhibiting a total negative GPP anomaly of −~~90.21~~22.55 Tg C yr^{-1} (Table S4) and a relative change of approximately 16%. Despite comparable relative changes in GPP for other provinces, their GPP anomalies are relatively smaller, within ~~ranging from −10 to −1~~5 Tg C yr^{-1}. Notably, Xinjiang, characterized by a fragile forest steppe in the Altai and Tianshan Mountain regions, consistently demonstrates substantial relative changes in GPP during both ENSO and other events. Quantitatively, during the El Niño episode, Xinjiang witnesses a remarkable 24% relative change in GPP, accompanied by a positive GPP anomaly of −3.82~~15.27~~ Tg C yr^{-1}. In contrast, during the La Niña episode, provinces with notable relative changes are mainly concentrated in the northern regions, such as Xinjiang, Inner Mongolia, Ningxia, Shanxi, and Liaoning provinces (Fig. 7b). In addition, although the influence of ENSO on GPP in the southern China is significant (Fig. 4), the total relative change through the year remains small due to the cancellation of positive and negative anomalies in different seasons.

In the pIOD classification, only the 2019 extreme event is considered, resulting in the relative change in GPP anomalies exceeding 10% in approximately half of the provinces. Notably, Jiangxi, Fujian, Guangxi, Guangdong, and Hainan experience reductions of more than 25% in GPP, with Jiangxi exhibiting the largest GPP anomaly of ~~−130~~ 31.50 Tg C yr^{-1}, Conversely, Shandong, Shanxi, and Henan witness increase of over 25% in GPP (Fig. 7c). During nIOD events, northern provinces generally exhibit negative relative changes, while southern provinces display positive relative changes.

In summary, the relative changes in total GPP anomalies at the provincial scale exhibit an east-west pattern in annual variation. Meanwhile, the influence of IOD events on GPP presents an opposing north-south pattern.

4. Discussion

4.1 Seasonal legacy effect

While the legacy effects of climate on subsequent vegetation have been widely confirmed (Bastos et al., 2020; Bastos et al., 2021), they were not fully accounted for in this study. During ENSO and IOD events, temperature and soil moisture vary with seasons, resulting in diverse conditions such as high temperature and drought, high temperature and wet, low temperature and drought, and low temperature and wet across different regions and seasons. Vegetation does not immediately respond to changes in climatic conditions change due to its environmental resistance and self-regulation. These legacy effects are complex and vary by region as ENSO or IOD events progress through different seasons.

Spring serves as a transitional period between the peak of the climatic event and the peak of the growing season, making it challenging to fully explain the spatial patterns of GPP anomalies in parts of northern China sole based on temperature and soil moisture. Higher temperatures during DJF in El Niño events (Fig. 2f) can advance the growing season, subsequently impacting vegetation in the following spring. Sanders-DeMott et al. (2020) have proved that a warm winter can enhance the photosynthetic capacity of vegetation in the subsequent spring. Additionally, Yan et al. (2023) quantified the influence of the preceding and contemporaneous climatic conditions on NEP during the 1997/98 El Niño and pIOD compound event, showing that legacy effects can counteract or even reverse the effects of contemporaneous climatic conditions.

4.21 The effect of compound ENSO and IOD events on China's GPP

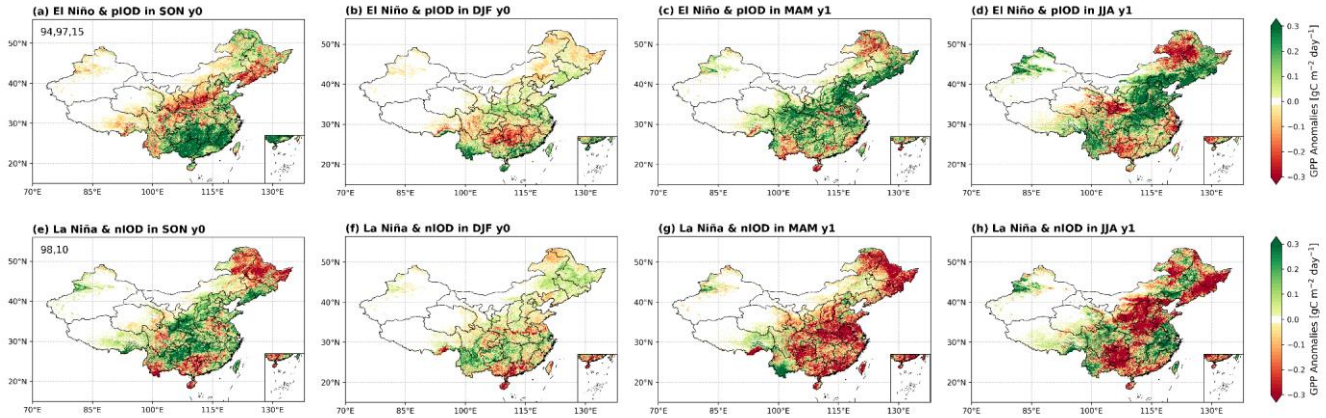

Fig. 8. Spatial distributions of seasonal composite GPP anomalies for compound events, (a-d) for El Niño & pIOD events, and (e-h) for La Niña & nIOD events. The two-digit year in first column denote the years used for composite analysis.

Indeed, despite IOD events being generally considered an independent coupled ocean-atmosphere interaction (Saji et al., 1999), historical IOD events can occur in conjunction with ENSO (Ham et al., 2017; Yang et al., 2015). These combined phenomena are most notable represented by El Niño & pIOD and La Niña & nIOD events. Williams and Hanan (2011) researched the interactive effects of ENSO and IOD on African GPP, relying on an offline terrestrial biosphere model simulation. Their findings suggested that IOD could cause obvious anomalous GPP over much of Africa, capable of suppressing or even reversing ENSO signals in GPP anomalies. In addition, Yan et al. (2023) explored the interactive effects of ENSO and IOD on seasonal anomalies of tropical net land carbon flux using the TRENDYv9 multi-model simulations, revealing diverse effects in different sub-continents and seasons. We explore the anomalies of GPP in compound events based on composite analysis (Fig. 8), and the spatial patterns of soil moisture and temperature anomalies are shown in the appendix (Figs. S9 and S10).

The spatial patterns of the GPP anomalies during concurrent ENSO and IOD events differ from those in single events, although some similarities are evident. GPP anomalies in El Niño & pIOD and La Niña & nIOD events are generally opposite, and we focus specifically on El Niño & pIOD events here. In El Niño & pIOD events, GPP anomalies exhibit a general opposition, with enhanced vegetation photosynthesis in the southern regions and inhibited in the northern regions during SON. This spatial characteristic of GPP anomalies bears some resemblance to that induced by El Niño alone (Figs. 4a and 8a). Weak GPP anomalies are generally observed in DJF, with noticeable negative GPP anomalies in Guizhou and Hunan, and some positive GPP anomalies in regions south of 25°N (Fig. 8b). Notably during DJF, while significant positive GPP anomalies occur in El Niño events (Fig. 4b), simultaneous pIOD events induce significant negative GPP anomalies (Fig. 5b). When both events coincide, their impacts seem to largely counterbalance each other, resulting in a more neutral GPP anomaly. In MAM, GPP increases in Northern China (Fig. 8c). Subsequently, in JJA, vegetation photosynthesis experiences a significant increase in the Northern and Yunnan provinces (Fig. 8d).

It is worth noting that the impacts of compound events on China's GPP may not follow a straightforward linear superposition of the effects of two individual events. While their effects are nearly opposite when occurring separately, the positive and negative effects on GPP may be not simply cancelled each other out when they coincide. This complexity arises from the simultaneous occurrence of two tropical air-sea interaction modes, leading to intricate effects on mid-latitude circulations. Given the limited number of compound events, further exploration is necessary to unravel the effects of ENSO and IOD on GPP in China.

4.3~~2~~ Modulation of large-scale circulations on China's GPP

China's GPP is intricately influenced by atmospheric circulations and sea surface temperature (Li et al., 2021; Ying et al., 2022). Ying et al. (2022) showed significant correlations between seasonal GPP variation in China and climate phenomena such as ENSO, Pacific Decadal Oscillation (PDO), and Arctic Oscillation (AO), based on the Residual Principal Component analysis. Their research indicated that these identified SST and circulation factors could account for 13%, 23% and 19% of the seasonal GPP variations in spring, summer and autumn, respectively. And Li et al. (2021) proved that GPP response to El Niño varied with PDO phases during the growing seasons of typical El Niño years. Although both studies emphasized the impact of ENSO on China's GPP and explored the roles of PDO and AO, the IOD was notably absent from their analyses. Contrastingly, our study sheds light on the significant influence of the extreme positive phase of IOD in 2019, showing a substantial negative GPP anomaly in southeastern China during SON, aligning with findings by Wang et al. (2021b). Moreover, the integration of partial correlation and composite analysis in our study elucidates the considerable impact of IOD on China's GPP within this context. Importantly, our research underscores the temporal and spatial variability in the effects of IOD and ENSO on GPP across different seasons and regions. This complexity in ocean–atmosphere teleconnections implies that other climate oscillations, such as Polar/Eurasia (polarEA) and Atlantic Multidecadal Oscillation (AMO), might also contribute to influencing China's GPP (Zhu et al., 2017), which

is still worthy of further analysis and research.

4.43 Uncertainties in BEPS Simulations

The simulation of China's GPP by BEPS is subject to several sources of uncertainty inherent in the model's structure, parameterizations, processes, and input data (Chen et al., 2012; Chen et al., 2017; He et al., 2021a; Liu et al., 2018; Wang et al., 2021a). Leaf Area Index (LAI), a crucial input for the BEPS model, is derived from global remote sensing data that inherently possess uncertainties in spatial distribution and trend changes. Previous studies have highlighted significant uncertainties in simulating carbon budget of global terrestrial ecosystems when employing different LAI remote sensing data (Chen et al., 2019; Liu et al., 2018). Foliage clumping index which is used to separate sunlit and shaded LAI can also cause some uncertainties in simulating GPP, because the current version of BEPS used the time-invariant satellite-derived clumping index (Chen et al., 2012). Biases in meteorological drivers, such as precipitation, can further result in considerable uncertainties in simulating terrestrial carbon cycle. The choice of precipitation products, for instance, has been shown to yield considerable differences in simulated net land-atmosphere carbon flux (Wang et al., 2021c). Moreover, BEPS model, like other terrestrial biosphere models, lacks consideration for vegetation adaptability to rising CO_2 concentration, potentially leading to an overestimation of the fertilization effect on GPP. In addition, the accuracy of simulations over agricultural areas is compromised in BEPS, as it only considers crops with a C3 photosynthetic pathway and overlooks C4 crops (He et al., 2017; He et al., 2021b; Ju et al., 2006). Although BEPS simulated GPP demonstrates relatively high consistency with the measured GPP of Yingke Station (CRO), located in the northwest of China, its accuracy lacks validation over the extensive farmlands in north and northeastern China where various crops are grown (Fig. S11). Agricultural operations, particularly irrigation, which can significantly impact GPP, are not considered in BEPS. He et al. (2021a) revealed extensive wetting signals over croplands in arid and semi-arid areas which exerted strong impacts on GPP and evapotranspiration simulations in BEPS after assimilating

the Soil Moisture Active Passive (SMAP) soil moisture product. Furthermore, photosynthetic key parameters, such as carboxylation capacity at 25°C ($V_{cmax,25}$), can largely determine the performance in simulating GPP. After assimilating the solar-induced chlorophyll fluorescence (SIF) from the Orbiting Carbon Observing Satellite-2 (OCO-2) to optimize $V_{cmax,25}$ of different plant functional types (PFTs) in BEPS, previous studies suggested the improvements in simulating GPP at regional and global scales to some extent (He et al., 2019; Wang et al., 2021a).

5. Conclusion

In this paper, we used partial correlation coefficients and composite analysis to investigate the impacts of ENSO and IOD events on China's GPP during 1981–2021. The partial correlation results reveal that the effects of ENSO and IOD on GPP and related climate in China exhibit distinct seasonal variations and are basically opposite. Specifically, during SON, significant negative *pcor* between GPP and ENSO is observed over the Tibetan Plateau, southwestern China, Loess Plateau, and Liaoning. In DJF, strongly positive *pcor* occurs over southern China, weakening in the subsequent MAM, albeit with some enhancements in northern Hebei and neighboring Inner Mongolia. The *pcor* then turns generally negative in JJA. In contrast, significant positive *pcor* between GPP and IOD is noted in southwestern and Northeast China during SON. Subsequently, widespread negative *pcor* appears during DJF, persisting significantly in most western and northern regions during MAM. In JJA, the *pcor* becomes significantly positive in southwestern, north and northeast China. Moreover, the correlation coefficients between GPP and climate show that GPP anomalies are primarily dominated by SM during ENSO events except MAM~~in JJA and SON~~, while temperature generally plays a more important role during IOD events except SON~~in in DJF and MAM~~.

The composite analysis results validate the patterns of GPP anomalies observed in the partial correlation. Generally, China's annual total GPP demonstrates modest positive anomalies in La

Niña and nIOD years, contrasting with minor negative anomalies in El Niño and pIOD years. This results from the counterbalancing effects, with significantly greater GPP anomalous magnitudes in DJF and JJA. Regionally, GPP anomalies fluctuate more in the Southern and Northern regions. The GPP anomaly in the Southern region dominates the national GPP variation, with the contribution of 68% to ENSO events and 46% to IOD events, respectively. On the provincial scale, western and northern provinces in experience larger relative annual variations during ENSO events, with magnitudes exceeding 10%, exhibiting a general east-west pattern. Conversely, provinces in the southern and Northern China witness larger relative changes during IOD events, showing an opposing north-south pattern. For instance, the 2019 extreme pIOD led to relative changes of over 25% in certain provinces in the south and north.

Author contributions

Jun Wang designed the experiments. Ran Yan processed the data, carried out the analysis and wrote the original manuscript. All the authors contributed to the writing of the paper.

Acknowledgement

The calculations in this paper have been done on the computing facilities in the High Performance Computing Center (HPCC) of Nanjing University. This study was supported by the Natural Science Foundation of China (Grants 42141005 and 42475129), and the Natural Science Foundation of Jiangsu Province, China (BK20221449).

Conflict of Interest

The authors declare no competing interests.

Data Availability

ERA5~~REA5~~ meteorological data are available at https://cds.climate.copernicus.eu/cdsapp#!/dataset/reanalysis-era5-single-levels?tab=overview. The remote-sensing GLOBMAP LAI data is available at https://zenodo.org/record/4700264#.YzvSYnZBxD8/. The carbon dioxide emissions data is available at https://gml.noaa.gov/webdata/ccgg/trends/co2/co2_mm_mlo.txt. Vegetation type data for BEPS simulations is obtained from https://lpdaac.usgs.gov/products/mcd12q1v006/. Soil texture data is available at https://data.tpdc.ac.cn/zh-hans/data/611f7d50-b419-4d14-b4dd-4a944b141175. Soil moisture and surface air temperature from ERA5-Land are available at https://cds.climate.copernicus.eu/cdsapp#!/dataset/reanalysis-era5-land-monthly-means?tab=overview. Sea surface temperature dataset from ERSSTv5 is available at https://psl.noaa.gov/data/gridded/data.noaa.ersst.v5.html. Eight sites of the ten are from ChinaFlux (http://www.chinaflux.org/enn/index.aspx), and two are from National Tibetan Plateau Third Pole Environment (http://data.tpdc.ac.cn/z

h-hans). FluxSat GPP Version 2.2 are available at https://avdc.gsfc.nasa.gov/pub/tmp/FluxSat_GPP.

Reference

Ahlstrom, A., Raupach, M. R., Schurgers, G., Smith, B., Arneth, A., Jung, M., Reichstein, M., Canadell, J. G., Friedlingstein, P., Jain, A. K., Kato, E., Poulter, B., Sitch, S., Stocker, B. D., Viovy, N., Wang, Y. P., Wiltshire, A., Zaehle, S., Zeng, N.: The dominant role of semi-arid ecosystems in the trend and variability of the land CO_2 sink, Science, 348(6237), 895-899, https://doi:10.1126/science.aaa1668, 2015.

Antonietta, C., Andrew, T., Matthew, N., Emanuele, Di., Jin-Yi, Y., Pascale, B., Julia, C., Boris, D., Benjamin G., Eric, G., Fei-Fe, J., Kristopher, K., Benjamin, K., Tong, L., Niklas, S., Yan, X., and Sang-Wook, Y.: Understanding ENSO Diversity, B. Am. Meteorol. Soc., 96(6), 921-938, https://doi:10.1175/BAMS-D-13-00117.1, 2015.

Bastos, A., Ciais, P., Friedlingstein, P., Sitch, S. and Zaehle, S.: Direct and seasonal legacy effects of the 2018 heat wave and drought on European ecosystem productivity. Sci. Adv., 6, eaba2724, https://doi.org/10.1126/sciadv.aba2724, 2020.

Bastos, A., Orth, R., Reichstein, M., Ciais, P., Viovy, N., Zaehle, S., Anthoni, P., Arneth, A., Gentine, P., Joetzjer, E., Lienert, S., Loughran, T., McGuire, P. C., O, S., Pongratz, J., and Sitch, S.: Vulnerability of European ecosystems to two compound dry and hot summers in 2018 and 2019, Earth Syst. Dynam., 12, 1015–1035, https://doi.org/10.5194/esd-12-1015-2021, 2021.

Bauch, M.,: Chapter 15 - Impacts of extreme events on medieval societies: Insights from climate history, in: Climate Extremes and Their Implications for Impact and Risk Assessment, edited by: Sillmann, J., Sippel, S., and Russo, S., Elsevier, 279-291,https://doi.org/10.1016/B978-0-12-814895-2.00015-X, 2020.

Chen, J., Liu, J., Cihlar, J., and Goulden, M.: Daily canopy photosynthesis model through temporal and spatial scaling for remote sensing applications, Ecol. Model., 124, 99–119, https://doi:10.1016/S0304-3800(99)00156-8, 1999.

Chen, J. M., Mo, G., Pisek, J., Liu, J., Deng, F., Ishizawa, M., and Chan, D.: Effects of foliage clumping on the estimation of global terrestrial gross primary productivity, Global Biogeochem. Cy., 26, GB1019, https://doi.org/10.1029/2010GB003996, 2012.

Chen, J., Ju, W., Ciais, P., Viovy, N., Liu, R., Liu, Y., and Lu X.: Vegetation structural change since 1981 significantly enhanced the terrestrial carbon sink, Nat. Commun., 10, 4259, https://doi:10.1038/s41467-019-12257-8, 2019.

Chen, Z., Chen, J., Zhang, S., Zheng, X., Ju, W., Mo, G., Lu, X.: Optimization of Terrestrial Ecosystem Model Parameters Using Atmospheric CO_2 Concentration Data With the Global Carbon Assimilation System (GCAS), J. GEOPHYS. RES. - BIOGEO., 122, 3218-3237, http://doi.org/10.1002/2016JG003716, 2017

Gough, C.: Terrestrial primary production: Fuel for life, Nature Education Knowledge, 3. 2012

Ham, Y., Choi, J., and Kug, J.: The weakening of the ENSO–Indian Ocean Dipole (IOD) coupling strength in recent decades, Clim. Dynam., 49(1), 249-261, https://doi:10.1007/s00382-016-3339-5, 2017.

He, B., Chen, C., Lin, S., Yuan, W., Chen, H., Chen, D., Zhang, Y., Guo, L., Zhao, X., Liu., Piao, S., Zhong, Z., Wang, R., and Tang, R.: Worldwide impacts of atmospheric vapor pressure deficit on the interannual variability of terrestrial carbon sinks, Natl. Sci. Rev., 9(4), nwab150, https://doi:10.1093/nsr/nwab150, 2022.

He, L., Chen, J., Liu, J., Bélair, S., and Luo, X.: Assessment of SMAP soil moisture for global simulation of gross primary production, J. Geophys. Res. – Biogeo., 122(7), 1549-1563, https://doi:10.1002/2016jg003603, 2017.

He, L., Chen, J., Liu, J., Zheng, T., Wang, R., Joiner, J., Chou, S., Cheng, B., Liu, Y., and Liu, R.: Diverse photosynthetic capacity of global ecosystems mapped by satellite chlorophyll fluorescence measurements, Remote Sens. Environ., 232, https://doi:10.1016/j.rse.2019.111344, 2019.

He, L., Chen J., Mostovoy, G., and Gonsamo, A.: Soil Moisture Active Passive Improves Global Soil Moisture Simulation in a Land Surface Scheme and Reveals Strong Irrigation Signals Over Farmlands, Geophys. Res. Lett., 48(8), https://doi:10.1029/2021gl092658, 2021a.

He, L., Wang, R., Mostovoy, G., Liu, J., Chen, J., Shang, J., Liu, J., McNairn, H., and Powers, J.: Crop

Biomass Mapping Based on Ecosystem Modeling at Regional Scale Using High Resolution Sentinel-2 Data, Remote Sens., 13(4), https://doi:10.3390/rs13040806, 2021b.

He, Q., Ju, W., Dai, S., He, W., Song, L., Wang, S., Li, X., and Mao, G.: Drought Risk of Global Terrestrial Gross Primary Productivity Over the Last 40 Years Detected by a Remote Sensing-Driven Process Model. J. Geophys. Res. – Biogeo., 126(6): e2020JG005944, 2021.

Hersbach, H., Bell, B., Berrisford, P., Biavati, G., Horányi, A., Muñoz Sabater, J., Nicolas, J., Peubey, C., Radu, R., Rozum, I., Schepers, D., Simmons, A., Soci, C., Dee, D., Thépaut, J-N.: ERA5 hourly data on single levels from 1940 to present, Copernicus Climate Change Service (C3S) Climate Data Store (CDS) [data set], https://doi: 10.24381/cds.adbb2d47, 2023.

Houghton, R. A.: Balancing the global carbon budget, Annu. Rev. Eart. Pl. Sc., 35, 313-347, https://doi:10.1146/annurev.earth.35.031306.140057, 2007.

Joiner, J., Yoshida, Y., Zhang, Y., Duveiller, G., Jung, M., Lyapustin, A., Wang, Y., and Tucker, C. J.: Estimation of Terrestrial Global Gross Primary Production (GPP) with Satellite Data-Driven Models and Eddy Covariance Flux Data, Remote Sens., 10(9), https://doi:10.3390/rs10091346, 2018.

Ju, W., Chen J., Black T., Barr, A., Liu, J., and Chen, B.,: Modelling multi-year coupled carbon and water fluxes in a boreal aspen forest, Agr. Forest Meteorol., 140(1-4), 136-151, https://doi:10.1016/j.agrformet.2006.08.008, 2006.

Fischer, G., Nachtergaele, F., Prieler, S., van Velthuizen, H. T., Verelst, L., Wiberg, D.: Global Agro-ecological Zones Assessment for Agriculture (GAEZ 2008), IIASA [data set], Laxenburg, Austria and FAO, Rome, Italy, 2008.

Friedl, M., Sulla-Menashe, D.: MCD12Q1 MODIS/Terra+Aqua Land Cover Type Yearly L3 Global 500m SIN Grid V006, NASA EOSDIS Land Processes Distributed Active Archive Center [data set], 2019.

Kim, J., Kug J., and Jeong S.: Intensification of terrestrial carbon cycle related to El Niño-Southern Oscillation under greenhouse warming, Nat. Commun., 8, https://doi:10.1038/s41467-017-01831-7, 2017.

Lan, X., Tans, P. and K.W. Thoning: Trends in globally-averaged CO_2 determined from NOAA Global Monitoring Laboratory measurements [data set], https://doi.org/10.15138/9N0H-ZH07, 2022.

Li, X., Cheng, G., Liu, S,, Xiao, Q., Ma, M., Jin, R., Che, T., Liu, Q., Wang, W., Qi, Y., Wen, J., Li, H., Zhu, G., Guo, J., Ran, Y., Wang, S., Zhu, Z., Zhou, J., Hu, X., Xu, Z.: Heihe watershed allied telemetry experimental research (HiWATER): scientific objectives and experimental design. Bull. Am. Meteorol. Soc. 94 (8), 1145–1160, https://doi.org/10.1175/BAMS-D-12-00154.1, 2013.

Li, Y., Dan, L., Peng, J., Wang, J., Yang, F., Gao, D., Yang, X., and Yu, Q.: Response of Growing Season Gross Primary Production to El Niño in Different Phases of the Pacific Decadal Oscillation over Eastern China Based on Bayesian Model Averaging, Adv. Atmos. Sci., 38(9), 1580-1595, https://doi:10.1007/s00376-021-0265-1, 2021.

Liu, J., Chen J., Cihlar, J., and Park W.: A process-based boreal ecosystem productivity simulator using remote sensing inputs, Remote Sens. Environ., 62(2), 158-175, https://doi.org/10.1016/S0034-4257(97)00089-8, 1997.

Liu, Y., Liu, R., and Chen, J.: Retrospective retrieval of long-term consistent global leaf area index (1981-2011) from combined AVHRR and MODIS data. J. Geophys. Res. Biogeosci. 117 (G4), G04003, https://doi.org/10.1029/2012JG002084, 2012.

Liu, Y., Xiao, J., Ju, W., Zhu, G., Wu, X., Fan,W., Li, D., and Zhou, Y.: Satellite-derived LAI products exhibit large discrepancies and can lead to substantial uncertainty in simulated carbon and water fluxes, Remote Sens. Environ., 206, 174-188, https://doi:10.1016/j.rse.2017.12.024, 2018.

Liu, Y., Yang X., Wang, E., and Xue, C.: Climate and crop yields impacted by ENSO episodes on the North China Plain: 1956-2006, Reg. Environ. Change., 14(1), 49-59, https://doi:10.1007/s10113-013-0455-1, 2014.

Mercado, L., Bellouin, N., Sitch, S., Boucher, O., Huntingford, C., Wild, M., Cox, P.: Impact of changes in diffuse radiation on the global land carbon sink, Nature, 458(7241), 1014-1017, https://doi:10.1038/nature07949, 2009.

Muñoz, S. J.: ERA5-Land monthly averaged data from 1950 to present. Copernicus Climate Change Service (C3S) Climate Data Store (CDS) [data set], 2019.

Norman, J. M.: Simulation of microclimates, in: Biometeorology in Integrated Pest Management, edited by: Hatfield, J., Thomason, I., 65–99, New York, CA: Academic Press, 1982.

Piao, S., Wang, X., Wang, K., Li, X., Bastos, A., Canadell, J., Ciais, P., Friedlingstein, P., and Sitch, S.:

789 Interannual variation of terrestrial carbon cycle: Issues and perspectives, Global Change Biol., 26(1),
790 300-318, https://doi:10.1111/gcb.14884, 2020.
791 Ryu, Y., Berry J., and Baldocchi, D.: What is global photosynthesis? History, uncertainties and
792 opportunities, Remote Sens. Environ., 223, 95-114, https://doi:10.1016/j.rse.2019.01.016, 2019.
793 Saji, N., Goswami, B, Vinayachandran P, and Yamagata, T.: A dipole mode in the tropical Indian Ocean,
794 Nature, 401(6751), 360-363, https://doi:Doi 10.1038/43855, 1999.
795 Saji, N., and Yamagata, T.: Possible impacts of Indian Ocean Dipole mode events on global climate,
796 Clim. Res., 25(2), 151-169, https://doi:10.3354/cr025151, 2003.
797 Sanders-DeMott, R., Ouimette, A., Lepine, L., Fogarty, S., Burakowski, E., Contosta, A., Ollinger, S.:
798 Divergent carbon cycle response of forest and grass-dominated northern temperate ecosystems to record
799 winter warming. Global Change Biol., 26(3): 1519-1531, https://doi.org/10.1111/gcb.14850, 2020.
800 Schimel, D., Stephens, B., and Fisher, J.: Effect of increasing CO_2 on the terrestrial carbon cycle, P.
801 Natl. Acad. Sci. USA., 112(2), 436-441, https://doi:10.1073/pnas.1407302112/-/DCSupplemental,
802 2015.
803 Wang, J., Zeng, N., and Wang, M.: Interannual variability of the atmospheric CO_2 growth rate: roles of
804 precipitation and temperature, Biogeo., 13(8), 2339-2352, https://doi:10.5194/bg-13-2339-2016, 2016.
805 Wang, J., Zeng, N., Wang, M., Jiang, F., Chen, J., Friedlingstein, P., Jain, A., Jiang, Z., Ju, W., Lienert,
806 S., Nabel, J., Sitch, S., Viovy, N., Wang, H., and Wiltshire, A.: Contrasting interannual atmospheric CO_2
807 variabilities and their terrestrial mechanisms for two types of El Niños, Atmos. Chem. Phys., 18(14),
808 10333-10345, https://doi:10.5194/acp-18-10333-2018, 2018.
809 Wang, J., Liu, Z., Zeng, N., Jiang, F., Wang, H., and Ju, W.: Spaceborne detection of XCO2 enhancement
810 induced by Australian mega-bushfires, Environ. Res. Lett., 15(12), https://doi:10.1088/1748-
811 9326/abc846, 2020.
812 Wang, J., Jiang. F., Wang. H., Qiu. B., Wu. M., He. W., Ju. W., Zhang. Y., Chen. J., and Zhou, Y.:
813 Constraining global terrestrial gross primary productivity in a global carbon assimilation system with
814 OCO-2 chlorophyll fluorescence data, Agr. Forest Meteorol., 304-305,
815 https://doi:10.1016/j.agrformet.2021.108424, 2021a.
816 Wang, J., et al.: Modulation of Land Photosynthesis by the Indian Ocean Dipole: Satellite-Based

817 Observations and CMIP6 Future Projections, Earth's Future, 9(4), https://doi:10.1029/2020ef001942.
818 2021b.
819 Wang, M., Wang, J., Cai, Q., Zeng, N., Lu, X., Yang, R., Jiang, F., Wang, H., and Ju, W.: Considerable
820 Uncertainties in Simulating Land Carbon Sinks Induced by Different Precipitation Products, J. Geophys.
821 Res. - Biogeo., 126(10), e2021JG006524, https://doi.org/10.1029/2021JG006524. 2021c
822 Wang, J., Jiang, F., Ju, W., Wang, M., Sitch, S., Arora, V., Chen, J., Goll, D., He, W., Jain, A., Li, X.,
823 Joiner, J., Poulter, B., Seferian, R., Wang, H.,Wu, M., Xiao, J., Yuan, W., Yue, X., Zaehle, S.: Enhanced
824 India-Africa Carbon Uptake and Asia-Pacific Carbon Release Associated With the 2019 Extreme
825 Positive Indian Ocean Dipole, Geophys. Res. Lett., 49(22), https://doi:10.1029/2022gl100950, 2022.
826 Wang, J., et al.,: Anomalous Net Biome Exchange Over Amazonian Rainforests Induced by the 2015/16
827 El Niño: Soil Dryness-Shaped Spatial Pattern but Temperature-dominated Total Flux, Geophys. Res.
828 Lett., 50(11), https://doi:10.1029/2023GL103379, 2023.
829 Williams, C., and Hanan, N.: ENSO and IOD teleconnections for African ecosystems: evidence of
830 destructive interference between climate oscillations, Biogeo., 8(1), 27-40, https://doi:10.5194/bg-8-
831 27-2011, 2011.
832 Yan, R., Wang, J., Ju, W., Goll, D., Jain, A., Sitch, S., Tian, H., Benjamin, P., Jiang, F., and Wang, H.:
833 Interactive effects of the El Niño-Southern Oscillation and Indian Ocean Dipole on the tropical net
834 ecosystem productivity, Agr. Forest Meteorol., 336, 109472,
835 https://doi.org/10.1016/j.agrformet.2023.109472, 2023.
836 Yang, R., Wang, J., Zeng, N., Sitch, S., Tang, W., McGrath, M., Cai, Q., Liu, D., Lombardozzi, D., Tian,
837 H., Jain, A., and Han, P.: Divergent historical GPP trends among state-of-the-art multi-model
838 simulations and satellite-based products, Earth Syst. Dynam., 13(2), 833-849, https://doi:10.5194/esd-
839 13-833-2022, 2022.
840 Yang, Y., S.-P. Xie, L. Wu, Y. Kosaka, N.-C. Lau, and G. A. Vecchi, 2015: Seasonality and Predictability
841 of the Indian Ocean Dipole Mode: ENSO Forcing and Internal Variability, J. Climate, 28(20), 8021-
842 8036, https://doi:10.1175/JCLI-D-15-0078.1.
843 Ying, K., Peng, J., Dan, L., and Zheng, X.: Ocean—atmosphere Teleconnections Play a Key Role in the
844 Interannual Variability of Seasonal Gross Primary Production in China, Adv. Atmos. Sci., 39(8), 1329-

1342, https://doi:10.1007/s00376-021-1226-4, 2022.

Zeng, N., Mariotti, A., and Wetzel, P.: Terrestrial mechanisms of interannual CO_2 variability, Global Biogeochem Cy., 19(1), https://doi:10.1029/2004gb002273, 2005.

Zhang, X., Wang, Y., Peng, S., Rayner, P., Ciais, P., Silver, J., Piao, S., Zhu, Z., Lu, X., Zheng, X.: Dominant regions and drivers of the variability of the global land carbon sink across timescales, Global Change Biol., 24(9), 3954-3968, https://doi:10.1111/gcb.14275, 2018.

Zhang, Y., Dannenberg, M., Hwang, T., and Song, C.: El Niño-Southern Oscillation-Induced Variability of Terrestrial Gross Primary Production During the Satellite Era, J. Geophys. Res. - Biogeo., 124(8), 2419-2431, https://doi:10.1029/2019jg005117, 2019.

Zhang, Y., Zhou, W., Wang, X., Wang, X., Zhang, R., Li, Y., and Gan, J.: IOD, ENSO, and seasonal precipitation variation over Eastern China, Atmos. Res., 270, https://doi:10.1016/j.atmosres.2022.106042, 2022a.

Zhang, Y., Zhou, W., Wang, X., Chen, S., Chen, J., and Li, S.: Indian Ocean Dipole and ENSO's mechanistic importance in modulating the ensuing-summer precipitation over Eastern China, NPJ Clim. Atmos. Sci., 5(1), https://doi:10.1038/s41612-022-00271-5, 2022b.

Zhu, Z., Piao, S., Xu, Y., Bastos, A., Ciais, P., and Peng, S.: The effects of teleconnections on carbon fluxes of global terrestrial ecosystems, Geophys. Res. Lett., 44(7), 3209-3218, https://doi:10.1002/2016GL071743, 2017.